Self-programming Synaptic Resistor Circuit for Intelligent Systems

*Christopher M. Shaffer, Atharva Deo, Andrew Tudor, Rahul Shenoy, Cameron D. Danesh, Dhruva Nathan, Lawren L. Gamble, Daniel J. Inman, and Yong Chen**

Dr. C. M. Shaffer, A. Deo, Dr. A. Tudor, R. Shenoy, Dr. C. D. Danesh, D. Nathan, and Prof. Y. Chen

Department of Mechanical and Aerospace Engineering, University of California, Los Angeles, California 90095, USA

E-mail: yongchen@seas.ucla.edu

Dr. L. L. Gamble, Prof. D. J. Inman

Aerospace Engineering Department, University of Michigan Ann Arbor, Michigan 48109, USA

Keywords: synaptic resistor, neuromorphic circuit, self-programming, artificial general intelligence

Abstract

Unlike artificial intelligent systems based on computers which need to be programmed for specific tasks, the human brain can “self-program” in real-time to create new tactics and adapt to arbitrary environments. Computers embedded in artificial intelligent systems can execute arbitrary signal-processing algorithms to outperform humans at specific tasks, but without the real-time self-programming functionality, they need to be preprogrammed by humans, fail in unpredictable environments beyond their preprogrammed domains, and lack general intelligence in arbitrary environments. In this work, a synaptic resistor circuit that can self-program in arbitrary and unpredictable environments in real-time is demonstrated. By integrating the synaptic signal-processing, memory, and correlative learning functions in each synaptic resistor, the synaptic resistor circuit can process signals and self-program the circuit concurrently in real-time with an energy efficiency about six-orders higher than those of computers. In comparison with humans and a preprogrammed computer, the self-programming synaptic resistor circuit dynamically modified its algorithm to control a morphing wing in an unpredictable aerodynamic environment to improve its performance function with superior self-programming speeds and accuracy. The synaptic resistor circuits can potentially circumvent the fundamental limitations of computers, leading to a new intelligent platform with real-time self-programming functionality for artificial general intelligence.

1. Introduction

The human brain has long served as the inspiration of artificial intelligent systems. A neural network (**Figure 1a**) processes voltage pulses at M presynaptic neurons inducing currents via synapses at N postsynaptic neurons by following the signal processing algorithm,

$$\boldsymbol{I} = \boldsymbol{w}\,\boldsymbol{x} \qquad (1)$$

where $\boldsymbol{w} = (w_{nm}) \in \mathbb{R}^{N\times M}$ denotes a matrix with w_{nm} as the weight (conductance) of a synapse connecting the mth presynaptic and the nth postsynaptic neuron, $\boldsymbol{x} = (x_m) \in \mathbb{R}^M$ denotes a vector with x_m as the voltage pulses at the mth presynaptic neuron, and $\boldsymbol{I} = (I_n) \in \mathbb{R}^N$ denotes a vector with I_n as the current flowing into the nth postsynaptic neuron, which triggers the voltage pulses $\boldsymbol{y} = (y_n) \in \mathbb{R}^N$ with y_n as the pulses output from the nth postsynaptic neuron. Concurrently, the synaptic weight matrix, $\boldsymbol{w}$, is modified by following the learning algorithm,[1, 2]

$$\dot{\boldsymbol{w}} = \alpha\,\boldsymbol{z} \otimes \boldsymbol{x} \qquad (2)$$

where α denotes the modification coefficient, $\boldsymbol{z} = (z_n) \in \mathbb{R}^N$ denotes a function of $\boldsymbol{y} = (y_n) \in \mathbb{R}^N$ with y_n as the voltage pulses at the nth postsynaptic neuron (Supporting Information, Equation S1), and $\boldsymbol{z} \otimes \boldsymbol{x}$ represents the outer product between $\boldsymbol{z}$ and $\boldsymbol{x}$. By integrating signal-processing, memory, and correlative learning functions in each synapse, a neural network concurrently executes the signal-processing (Equation 1) and learning (Equation 2) algorithms in analog parallel mode to dynamically self-program $\boldsymbol{w}$ and create new functions in real-time in unpredictable and arbitrary environments with general intelligence.[1, 3, 4]

Computers embedded in artificial intelligent systems can execute arbitrary signal-processing algorithms[5] to outperform humans at specific tasks such as pattern recognition[6] and the Go game,[7] but they need to be preprogrammed by humans, and cannot adapt or develop new functions in unpredictable and arbitrary environments as humans do.[4] The time and energy consumption to compute machine learning algorithms from a dataset with M-dimensional variables increase versus M exponentially,[8] referred to as the "curse of dimensionality",[9] therefore learning algorithms are executed in off-site high-speed computers with high-power consumptions and bulky volumes.[7, 10, 11] Despite improved parallelism and computational energy efficiencies, transistor-based computing circuits, such as the Summit supercomputer,[12] graphics processing units (GPUs),[7, 11, 13] tensor processing units (TPUs),[14] field-programmable gate arrays (FPGAs),[15] TrueNorth[16] and Tianjic[17] neuromorphic circuits, are still based on the Turing computing model by executing algorithms with data transmissions between physically separated logic and memory transistors. Existing neuromorphic devices such as transistors,[18, 19] memristors,[20, 21] and phase change memory resistors,[22] execute signal-processing algorithms (without conductance change) and learning algorithms (with conductance change) by applying voltage pulses with different amplitudes. To avoid change of conductance during signal-processing, the voltage pulses for signal-processing are decreased to smaller magnitudes than the voltage pulses for learning. When the signal-processing algorithm is executed in the circuits, the learning algorithm is interrupted, and vice versa[22-25]. Therefore, unlike neurobiological networks, the existing neuromorphic circuits cannot execute signal-processing and learning algorithms concurrently, and need to be trained or preprogrammed before executing signal-processing algorithms. Due to these limitations, the energy efficiencies for existing electronic circuits to compute learning algorithms are limited to the range of $\sim 10^7 - 10^{13}\ OPS/W$ (operations per second per watt),[7, 11-17, 20, 22, 24] which are significantly lower than that of the human brain ($\sim 10^{15}\ OPS/W$),[26] and largely prevent artificial intelligent systems from self-programming on site in real-time. Without real-time self-programming functionality, artificial intelligent systems fail in unpredictable environments beyond their preprogrammed domains,[27] and lack the brain-like general intelligence in arbitrary environments.[4]

Recently we have developed a synaptic resistor,[28] abbreviated as synstor hereinafter, to emulate a synapse. A synstor processes voltage pulses $\boldsymbol{x}$ by following $\boldsymbol{I} = \boldsymbol{w}\,\boldsymbol{x}$, Equation 1, and learns from voltage pulses $\boldsymbol{x}$ and $\boldsymbol{z}$ by following $\dot{\boldsymbol{w}} = \alpha\, \boldsymbol{z} \otimes \boldsymbol{x}$, Equation 2.

Unlike existing electronic devices such as transistors, memristors, and phase change memory resistors, the synstors process and learn from the $\boldsymbol{x}$ and $\boldsymbol{z}$ voltage pulses with the same magnitudes, and the signal-processing ($\boldsymbol{I} = \boldsymbol{w}\, \boldsymbol{x}$, Equation 1) and learning ($\dot{\boldsymbol{w}} = \alpha\, \boldsymbol{z} \otimes \boldsymbol{x}$, Equation 2) algorithms can be executed concurrently in a synstor circuit without interrupting each other. A synstor circuit circumvents the energy consumption on data transmission and memory between logic and memory circuits for executing the signal-processing and learning algorithms separately in conventional computing circuits, and facilitates computations in analog parallel mode by integrating signal-processing, memory, and correlative learning functions in each synstor. In this article, we demonstrate a synstor-based self-programming neuromorphic integrated circuit (abbreviated as SNIC hereinafter) based on synstors (Figure 1a), which executes the signal processing ($\boldsymbol{I} = \boldsymbol{w}\, \boldsymbol{x}$, Equation 1) and correlative learning[1, 3] ($\dot{\boldsymbol{w}} = \alpha\, \boldsymbol{z} \otimes \boldsymbol{x}$, Equation 2) algorithms concurrently in parallel analog mode to self-program the synstor conductance matrix, $\boldsymbol{w}$, toward its optimal values, $\widehat{\boldsymbol{w}}$, and improve the performance function of a system spontaneously with an energy efficiency ($\sim 3.3 \times 10^{17}\ OPS/W$) significantly higher than the energy efficiencies of computing circuits (~$10^{7} - 10^{13}\ OPS/W$)[7, 11-16, 20, 22, 24] and the human brain ($\sim 10^{15}\ OPS/W$).[26]

2. Experiment and Results

We fabricated a crossbar synstor circuit (Supporting Information, **Figure S1**), and each synstor[28] has a p-type semiconducting carbon nanotube (CNT) channel which forms Schottky contacts with Al input and output electrodes as a resistor. A $HfO_2/TiO_2/HfO_2$ charge trap heterojunction is sandwiched between the CNT channel and a grounded Al reference electrode as a capacitor (Supporting Information, **Figure S2**). As shown in Figure 1a, voltage pulses, x_m, on the input electrodes induce currents flowing through the CNT channels to the n^{th} output neuron circuit by following the signal-processing algorithm, $I_n = \sum_m w_{nm} x_m$ (Equation 1). When paired negative (positive) voltage pulses, x_m and z_n, are applied on the m^{th} input and n^{th} output electrodes of a synstor simultaneously, the pulses generate a potential difference between the CNT channel and the TiO_2 charge storage layer to drive electrons to hop through the HfO_2 dielectric layer, increasing the negative (positive) charge stored in the charge storage layer, and in turn attracting (repelling) the holes in the p-type CNT channel to increase (decrease) the synstor conductance by following the learning algorithm, $\dot{w}_{nm} = \alpha\, z_n\, x_m$ (Equation 2), with $\alpha > 0$ ($\alpha < 0$). Otherwise, when $z_n = 0$ and/or $x_m = 0$, the x_m or z_n voltage pulse mainly drops beyond the recessed TiO_2 charge storage layer, and the potential difference between the CNT channel and the TiO_2 charge storage layer are below the threshold values to modify the charge stored in the charge storage layer, so $\dot{w}_{nm} = \alpha\, z_n\, x_m = 0$ (Supporting Information, **Figure S3** and **S4**). The synstor circuit executes the signal processing ($\boldsymbol{I} = \boldsymbol{w}\,\boldsymbol{x}$, Equation 1) and correlative learning ($\dot{\boldsymbol{w}} = \alpha\, \boldsymbol{z} \otimes \boldsymbol{x}$, Equation 2) algorithms concurrently without interrupting each other (Experimental Section).

To test SNIC in a practical challenging environment, a SNIC composed of a 2 × 2 crossbar synstor circuit, and 2 input and 2 output integrate-and-fire neuron circuits was connected to a morphing wing[29, 30] in a wind tunnel (**Figure** 1a and **1b**, Experimental Section). The synstor conductance matrix, $\boldsymbol{w}$, had random values before a self-programming process, and the goal was to set $\boldsymbol{w}$ in the real-time self-programming process to tune the lift-force on the wing, F, toward the target value, $\hat{F} = 0.3\ N$, and minimize an objective function $E = \frac{1}{2}\left(F - \hat{F}\right)^2$. The wind speed, S, changed randomly in the wind tunnel in the range of $17 - 29\ m/s$ to emulate an unpredictable aerodynamic environment which caused the lift-force on the wing, F, to vary randomly in the range of $0 - 1\ N$. F was also influenced by the shape of the wing, which was controlled by a voltage, V_a, applied on a piezoactuator in the wing (Figure 1b, Experimental Section). F was detected by a sensor in the wind tunnel, and the sensory signals were processed by input neurons to trigger $10\ ns$-wide input voltage pulses, $\boldsymbol{x}$, with an amplitude of $1.5\,V$ or $-1.75\,V$ (**Figure 2a**). When $F > \hat{F}$, the pulses were triggered from the 1^{st} input neuron only; when $F < \hat{F}$, the pulses were triggered from the 2^{nd} input neuron only. The firing rates of the $\boldsymbol{x}$ input pulses were a nonlinear monotonically increasing sigmoid function of $\left|F - \hat{F}\right|$ (Experimental Section, Supporting Information, **Figure S5**). $\boldsymbol{x}$ induced currents $\boldsymbol{I}$ via the synstor circuit by following Equation 1, $\boldsymbol{I} = \boldsymbol{w}\,\boldsymbol{x}$, and $\boldsymbol{I}$ flowed into integrate-and-fire output neuron circuits to generate output pulses, $\boldsymbol{y}$, and feedback pulses, $\boldsymbol{z}$, at the output electrodes of the circuit. The firing rates of the $\boldsymbol{y}$ and $\boldsymbol{z}$ pulses were nonlinear monotonically increasing functions of $|\boldsymbol{I}|$ (Experimental Section, Supporting Information, **Figure S6**). The actuation voltage, V_a, was modified by $\boldsymbol{y}$ following $\dot{V}_a = \rho\left(r_{y1} - r_{y2}\right)$ with r_{y1} and r_{y2} as the firing rates of output pulses from the first and second output neurons, respectively, and $\rho = 8\,mV$. V_a was applied on a piezoactuator to modify the wing shape, lift-force F, and objective function E (**Figure 1c**). A wave of $10\,ns$-wide $1.5\,V$ $(-1.75\,V)$ $\boldsymbol{z}$ pulses were triggered at the first (second) output electrodes at $\sim 575\,ms$ before a wave of $\boldsymbol{y}$ pulses were triggered, and a train of $10\,ns$-wide $-1.75\,V$ $(1.5\,V)$ $\boldsymbol{z}$ pulses was triggered at the first (second) output electrodes at $\sim 575\,ms$ after the train of $\boldsymbol{y}$ pulses were triggered.(**Figure 2a**, Experimental Section, Equation S1). The time-shifts between $\boldsymbol{y}$ and $\boldsymbol{z}$ pulses were mainly set to accommodate the system time delay between the wing and SNIC. The synstor conductance matrix $\boldsymbol{w}$ was modified by the $\boldsymbol{z}$ and $\boldsymbol{x}$ voltage pulses by following the learning algorithm, $\dot{\boldsymbol{w}} = \alpha\,\boldsymbol{z} \otimes \boldsymbol{x}$ (Equation 2) in the real-time self-programming process to change V_a and minimize the objective function E under the wind conditions with randomly varied speed S (Figure 1c).

To compare the self-programming processes between SNIC and the human brain, 14 human participants without any pre-knowledge about the morphing wing and its control system received $F - \hat{F}$ signals visually, and were instructed to minimize the difference between F and $\hat{F}$, and the objective function $E = \frac{1}{2}\left(F - \hat{F}\right)^2$ by sending output signals $\boldsymbol{y}$ by pressing two keys preset randomly in a keyboard to increase or decrease the actuation voltage V_a on the wing (**Figure 1d and 2b**, Experimental Section). In the real-time self-programming processes, E was reduced by dynamically modifying V_a under wind with the same randomly varied speed S as that in the SNIC trials (Figure 1c). To compare the self-programming control processes by SNIC and human brains with control processes by a preprogrammed computer, a proportional-integral-derivative (PID) controller implemented on a computer received $F - \hat{F}$ signals, and output V_a signals to modify the wing shape and F (**Figure 1e**). The PID controller with various gains was tested to control V_a and the shape of the wing experiencing a wind with a static speed $S = 28.7\ m/s$, and the optimal PID gains leading to the minimal average E were identified (Supporting Information, **Figure S7**). After the PID controller was preprogrammed to the optimal gains, the PID controller modified the shape of the wing while experiencing wind with the same randomly varied speed S as that in the SNIC and human trials, emulating an unpredictable aerodynamic environment beyond the preprogrammed condition (Figure 1e and 2c).

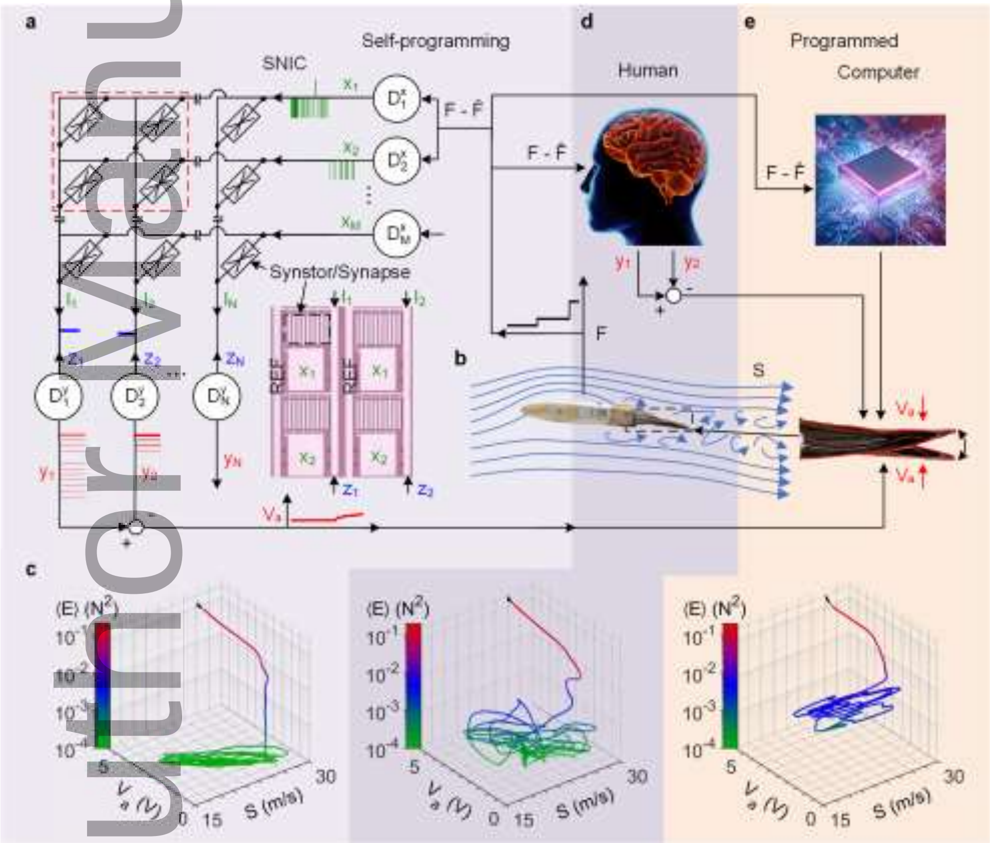

Figure 1. a) A schematic of a SNIC (a neural network) composed of $M \times N$ synstors (synapses) connected with M input (presynaptic) neurons, $D_1^i, D_2^i, \dots, D_M^i$, and N output (post-synaptic) neurons, $D_1^o, D_2^o, \dots, D_N^o$. A 2 × 2 crossbar synstor circuit is marked by dashed line, and shown in a microscope image in the inset. b) Left, an image of the morphing wing in wind (as illustrated by streamlines) with a randomly varied speed S to generate a lift force F on the wing. Right, a photo shows that the trailing

edge of the morphing wing is deflected upward by decreasing V_a, and downward by increasing V_a to modify F toward its target value $\hat{F}$. c) The average objective function $\langle E\rangle = \frac{1}{2}\langle (F - \hat{F})^2\rangle$ is plotted versus S and V_a in the typical morphing wing control processes by SNIC (left), human (middle), and computer (right). The black arrows indicate the evolving directions of the system. The illustration of d) a human, and e) a computer receiving $F - \hat{F}$ signals and adjusting V_a to modify wing shapes.

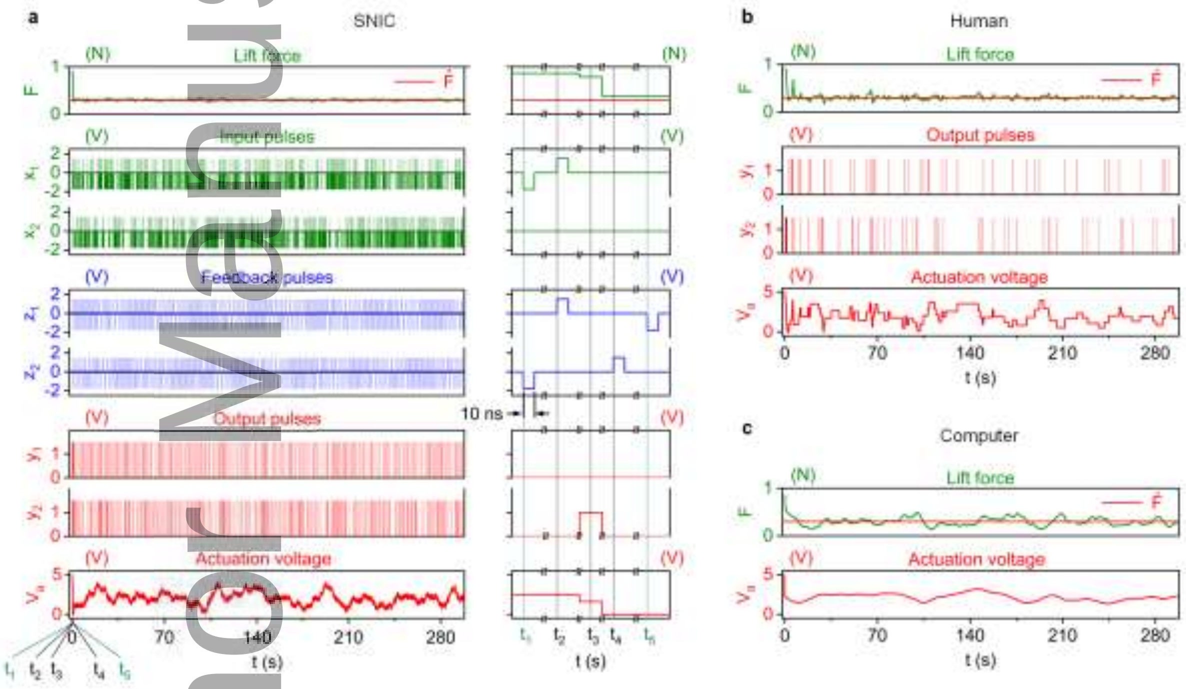

Figure 2. a) The lift force on the wing F, its target value $\hat{F}$, input voltage pulses x_m, feedback voltage pulses z_n, output voltage pulses y_n, and V_a in a typical trial by SNIC are plotted versus time t (left) and at moments t_1, t_2, t_3, t_4, and t_5 equal to 0.498, 0.516, 0.549, 1.080, and 1.099 s, respectively (right). F, $\hat{F}$, y_n, and V_a are plotted versus t in typical trials by b) human, and c) a computer.

3. Self-programming Process

In a SNIC or human self-programming process, when $F = \hat{F}$, $E = 0$, $\boldsymbol{x} = 0$, and $\dot{\boldsymbol{w}} = \alpha\, \boldsymbol{z} \otimes \boldsymbol{x} = 0$ (Equation 2), $\boldsymbol{w}$ reaches an equilibrium state $\widehat{\boldsymbol{w}} = arg \min_{\boldsymbol{w}} E$. Although $\boldsymbol{w}$ and $\widehat{\boldsymbol{w}}$ were not experimentally measured, the relative deviation of effective $\boldsymbol{w}$ from $\widehat{\boldsymbol{w}}$, $\Delta\boldsymbol{w}(t) = [\boldsymbol{w}(t) - \widehat{\boldsymbol{w}}]/|\boldsymbol{w}(0) - \widehat{\boldsymbol{w}}|$ was extrapolated (Supporting Information, Equation S2). The average E over a fixed moving time window, $\langle E \rangle$, is shown versus t in **Figure 3a**, versus $\Delta\boldsymbol{w}$ and the wind speed S in **Figure 3b**, and versus $|\Delta\boldsymbol{w}|$ in **Figure 3c**. Although $\boldsymbol{w}$ for SNIC and humans was not preprogrammed, and had random positive or negative initial deviations from $\widehat{\boldsymbol{w}}$, $\boldsymbol{w}$ was modified to $\widehat{\boldsymbol{w}}$, decreasing $\langle E \rangle$ toward equilibrium values, E_{eq}, within $\sim 5.1\ s$ for SNIC and $\sim 10\ s$ for humans in their self-programming processes. When the wind speed S changed chaotically, leading to increases of $|\Delta\boldsymbol{w}|$ and E, $\boldsymbol{w}$ was spontaneously modified toward $\widehat{\boldsymbol{w}}$ under the varied S, decreasing $\langle E \rangle$ monotonically versus t in the self-programming processes (Figure 3). The dynamic change of E in the self-programming process can be expressed as (Supporting Information, **Theorem 1**),

$$\langle \dot{E} \rangle = -\beta \langle E \rangle + \delta E \qquad (3)$$

where $\beta \geq 0$, and δE is related to the environmental influence and nonlinear term of E. In the self-programming processes for SNIC and human, $\delta E < \beta\langle E \rangle$, and $\langle \dot{E} \rangle = -\beta\langle E \rangle + \delta E\ < 0$, thus $\langle E \rangle$ represented a Lyapunov function, and was asymptotically decreased toward its dynamic equilibrium value E_{eq}, leading $\langle \boldsymbol{w} \rangle$ to be modified toward $\langle \widehat{\boldsymbol{w}} \rangle$ in the self-programming process; when $\delta E = \beta\langle E \rangle$, $\langle \dot{E} \rangle = 0$ and $\langle E \rangle$ reached its dynamic equilibrium value $E_{eq} = \delta E/\beta$ under $\langle \boldsymbol{w} \rangle = \langle \widehat{\boldsymbol{w}} \rangle$. The solution of Equation 3 gives, $\langle E \rangle = E_{eq} + (\langle E \rangle - E_{eq})e^{-\beta t} + \delta E * e^{-\beta t}$, where $\delta E * e^{-\beta t}$ represents the convolution between δE and $e^{-\beta t}$. When $\beta t \gg 1$, $\langle E \rangle \approx E_{eq}$, thus β represents the self-programming speed to modify $\langle E \rangle$ toward E_{eq}, and $\boldsymbol{w}$ toward $\widehat{\boldsymbol{w}}$ (Equation S5 in Supporting Information). With its gains preprogrammed to their optimal values under a static wind speed, the

PID controller decreased E initially, but the gains was not modified toward their optimal values dynamically under the varied S, leading to E significantly larger than those of the SNIC and humans (Figure 1c).

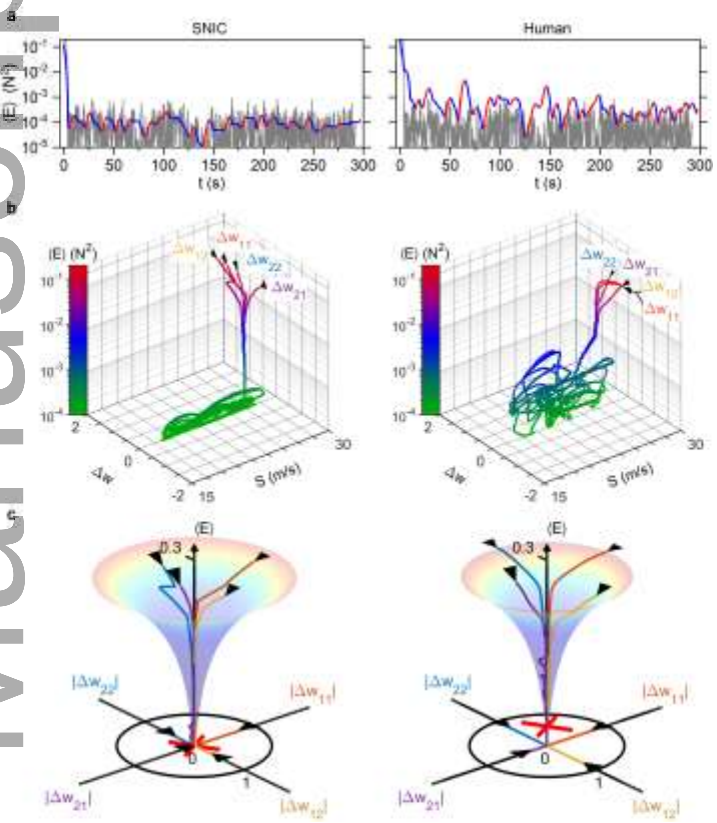

Figure 3. In the real-time self-programming processes of a SNIC (left) and human (right), a) objective functions E are shown versus t in gray color, and average objective functions, $\langle E\rangle$, are displayed versus time t in blue when $d\langle E\rangle/dt < 0$, and in red when $d\langle E\rangle/dt > 0$. b) $\langle E\rangle$ is plotted versus the relative deviations of the device conductances from the optimal conductances, Δw_{11}, Δw_{12}, Δw_{21}, and Δw_{22} and wind speed, S. c) $\langle E\rangle$ is plotted at logarithmic scale in 3D plots versus $|\Delta w_{11}|$, $|\Delta w_{12}|$, $|\Delta w_{21}|$, and $|\Delta w_{22}|$ at different azimuthal angles in linear scale. The evolving directions of Δw are indicated by arrows at the base planes of the 3D plots. $\langle E\rangle$ versus $\langle \Delta \boldsymbol{w}\rangle$ is best-fitted by $\langle E\rangle = \frac{1}{2}g^{E/\boldsymbol{w}}\langle \Delta \boldsymbol{w}\rangle^2 + E_{eq}$, and shown as 3D surfaces, with E_{eq} marked by red crosshairs.

In a self-programming process, β in Equation 3 represents the speed to reduce $\langle E \rangle$ toward E_{eq}, and modify $\boldsymbol{w}$ toward $\widehat{\boldsymbol{w}}$ (Supporting Information, Equation S5). As shown in **Figure 4a**, β increases with increasing average change rate of $\boldsymbol{w}$ at the initial stage of the self-programming process, $\langle |\dot{w}| \rangle^{i}$, which can be increased by increasing the firing rates of $\boldsymbol{x}$, $\boldsymbol{y}$, and $\boldsymbol{z}$ pulses, and decreasing the capacitances and leakage currents in the input and output neurons in SNIC (Supporting Information, **Figure S5** and **S6**). The equilibrium objective function E_{eq} defined in Equation 3 represents the accuracy to modify $\boldsymbol{w}$ toward $\widehat{\boldsymbol{w}}$ (Supporting Information, Equation S3). As shown in **Figure 4b**, E_{eq} reached its minimal values (data points 2 and 5) when the average change rate of $\boldsymbol{w}$ near the equilibrium stage of the self-programming process, $\langle |\dot{w}| \rangle^{e} = 0.62/s$ for SNIC, and $\langle |\dot{w}| \rangle^{e} = 0.32/s$ for humans. When $\langle |\dot{w}| \rangle^{e}$ is decreased from its optimal values (data points 1 and 4), the β value is decreased, and $E_{eq} = \delta E/\beta$, leading to the increase of E_{eq} since $E_{eq} = \delta E/\beta$. When β is decreased to zero in a control experiment without $\boldsymbol{z}$ pulses or self-programming, $\langle \dot{E} \rangle = \delta E > 0$ (Equation 3, and E_{eq} reaches the maximal value in Figure 4b. When $\langle |\dot{w}| \rangle^{e}$ is increased from its optimal values (data points 3 and 6), $\boldsymbol{w}$ is modified at a high rate, and $\boldsymbol{w}$ overshoots with respect to $\widehat{\boldsymbol{w}}$ near $\widehat{\boldsymbol{w}}$, leading to the fluctuation of $|\Delta \boldsymbol{w}|$ and E, and the increase of E_{eq} (**Figure 4c** and **4d**). In the self-programming processes, when $\boldsymbol{w}$ is close to $\widehat{\boldsymbol{w}}$, the pulse firing rates are decreased by the leakage current in the integrate-and-fire neuron circuits to avoid the overshoot of $\boldsymbol{w}$ with respect to $\widehat{\boldsymbol{w}}$, and reduce E_{eq}; when $\boldsymbol{w}$ deviates from $\widehat{\boldsymbol{w}}$, the pulse firing rates are increased as a nonlinear function of input signals to the neuron circuits to increase β and decrease E at high speed (Supporting Information, Figure S5 and S6). By optimizing the neuron circuits in SNIC, the average self-programming speed β ($0.46\ s^{-1}$) and E_{eq} ($7.2 \times 10^{-5}\ N^{2}$) in the self-programming process of SNIC are superior to β ($0.37\ s^{-1}$) and E_{eq} ($3.4 \times 10^{-4}\ N^{2}$) of the humans (Figure 3 and 4).

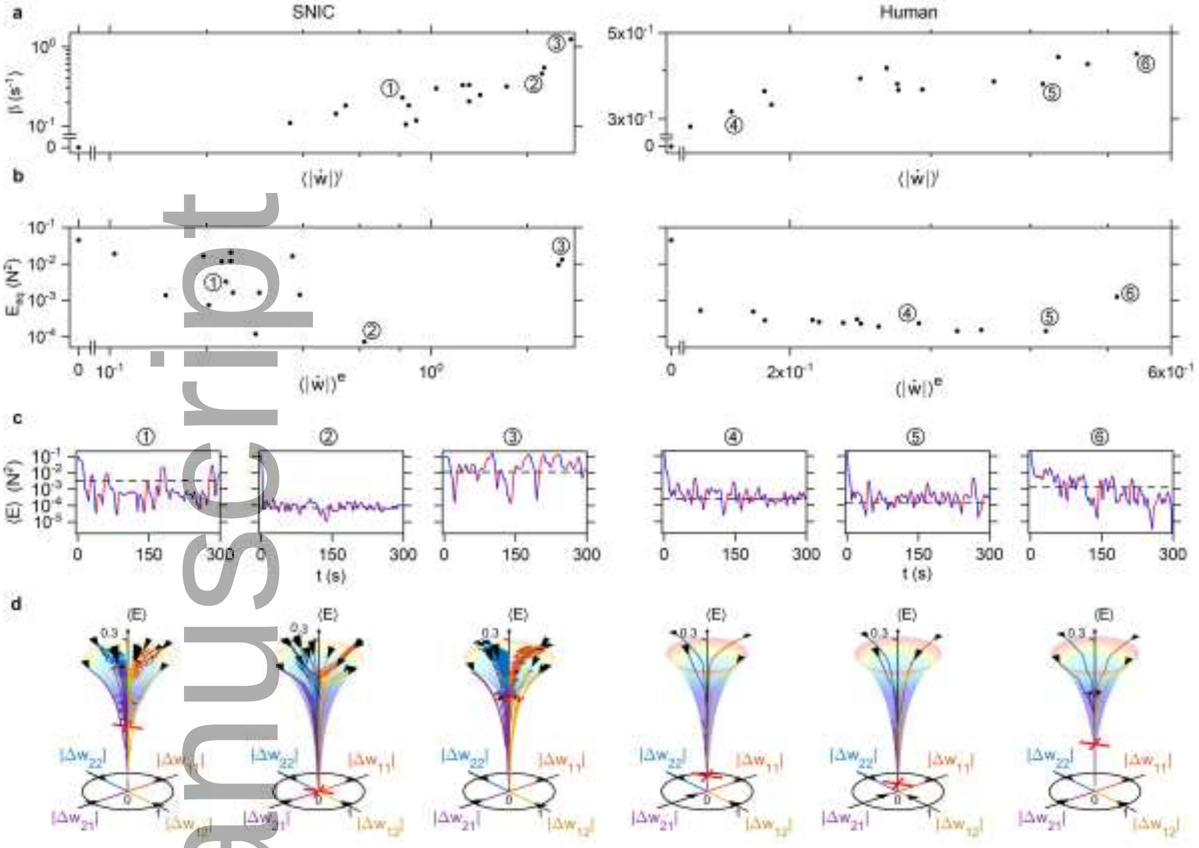

Figure 4. a) Learning speeds β and b) equilibrium objective functions E_{eq} are plotted versus the modification rates of their relative conductance matrix at the initial stages, $\langle|\dot{w}|\rangle^{i}$, and equilibrium stages, $\langle|\dot{w}|\rangle^{e}$, of the self-programming processes of (left) SNICs with different neuron circuits and (right) different humans. In the self-programming processes of (left) SNICs and (right) humans with different $\langle|\dot{w}|\rangle^{i}$ and $\langle|\dot{w}|\rangle^{e}$ (as marked by 1, 2, 3, 4, 5, and 6), c) average objective functions $\langle E\rangle$ are plotted versus time t in blue when $d\langle E\rangle/dt < 0$, and in red when $d\langle E\rangle/dt > 0$, and d) $\langle E\rangle$ is plotted at logarithmic scale in 3D plots versus $|\Delta w_{11}|$, $|\Delta w_{12}|$, $|\Delta w_{21}|$, and $|\Delta w_{22}|$, which are shown versus time at the base planes of the 3D plots, at different azimuthal angles by blue, red-orange, yellow, and violet lines, respectively. The arrows at the starting points of the lines indicate the evolving directions. $\langle E\rangle$ is best-fitted as a function $\Delta\boldsymbol{w}$ by $\langle E\rangle = \frac{1}{2}g^{E/\boldsymbol{w}}\langle\Delta\boldsymbol{w}\rangle^{2} + E_{eq}$, and shown in 3D surfaces, with $\langle E_{eq}\rangle$ marked by red crosshairs in d) and dashed lines in c).

4. Conclusion

In summary, we have demonstrated a self-programming neuromorphic integrated circuit (SNIC) based on synstors to emulate a neurobiological network based on synapses to execute the signal processing ($\boldsymbol{I} = \boldsymbol{w}\,\boldsymbol{x}$, Equation 1) and correlative learning ($\dot{\boldsymbol{w}} = \alpha\,\boldsymbol{z} \otimes \boldsymbol{x}$, Equition 2) algorithms concurrently in parallel analog mode. Unlike a programmable computer, the synstor conductance matrix $\boldsymbol{w}$ does not need to be preprogrammed, and can be spontaneously modified toward the optimal matrix $\widehat{\boldsymbol{w}}$, minimizing the objective function E in a self-programming process in complex and unpredictable environments. A SNIC controlled a morphing wing, modified its lift force F toward a targeted value $\hat{F}$, and minimized the objective function $E = \frac{1}{2}\left(F - \hat{F}\right)^2$ toward its equilibrium value E_{eq} in a wind with randomly varied speeds. The correlative learning algorithm executed in the synstor circuit can be extended to various learning algorithms include supervised, unsupervised, and reinforcement learning algorithms, leading to the optimization of predefined or self-organized objective functions in intelligent systems[3, 31]. Unlike artificial intelligent systems based on computers which need to be preprogrammed for specific tasks, SNIC does not need to be preprogrammed, and can "self-program" heuristically by executing the correlative learning algorithm in real-time in arbitrary environments for general intelligence. The real-time learning algorithm In comparison with humans and a preprogrammed computer, a SNIC demonstrated self-programming speeds and E_{eq} superior to those of the humans and computer. SNIC circumvents the energy consumptions on data transmissions in conventional computing circuits, facilitating a computing energy efficiency of $\sim 3.3 \times 10^{17}\ \ OPS/W$ (Experimental Section, Equation 6, **Figure 5**) significantly higher than the energy efficiencies of computing circuits ($\sim 10^7 - 10^{13}\ OPS/W$)[7, 11-16, 20, 22, 24] and the human brain ($\sim 10^{15}\ OPS/W$).[26] The speed to compute parallel signal processing and learning algorithms in a SNIC increases linearly with increasing circuit scale (Experimental Section, Equation 4, **Figure 5**), the power consumption of a SNIC increases with increasing circuit scale (Experimental Section, Equation 5), and the computing energy efficiency of a SNIC approximately does not change with increasing circuit scale (Experimental Section, Equation 6, **Figure 5**). A circuit of 10^6 synstors will have a speed ($6 \times 10^{14}\ \ OPS$) comparable with the speeds

(~$10^{12} - 10^{14}$ OPS) of TPU, GPU, and FPGA circuits with ~$10^{9} - 10^{11}$ transistors, and consume much less power ($\sim 30\ \mu W$) than those of the transistor-based circuits (~$40\ W$).[13-15] A circuit of 10^{9} synstors will have a speed (6×10^{16} OPS) comparable with the speeds of the human brain (~10^{16} OPS) and the Summit supercomputer (~10^{17} OPS), and consumes a power ($\sim 40\ mW$) much less than those of the human brain (~$30\ W$ with ~10^{14} synapses)[26] and Summit supercomputer (~10^{7} W with ~10^{14} transistors).[12] There is "plenty of room at the bottom" to scale up synstor circuits with high speed, low power consumption, high energy efficiency, and small circuit scale/volume for a new computing platform that can self-program in real-time in arbitrary and unpredictable environments for artificial general intelligence.

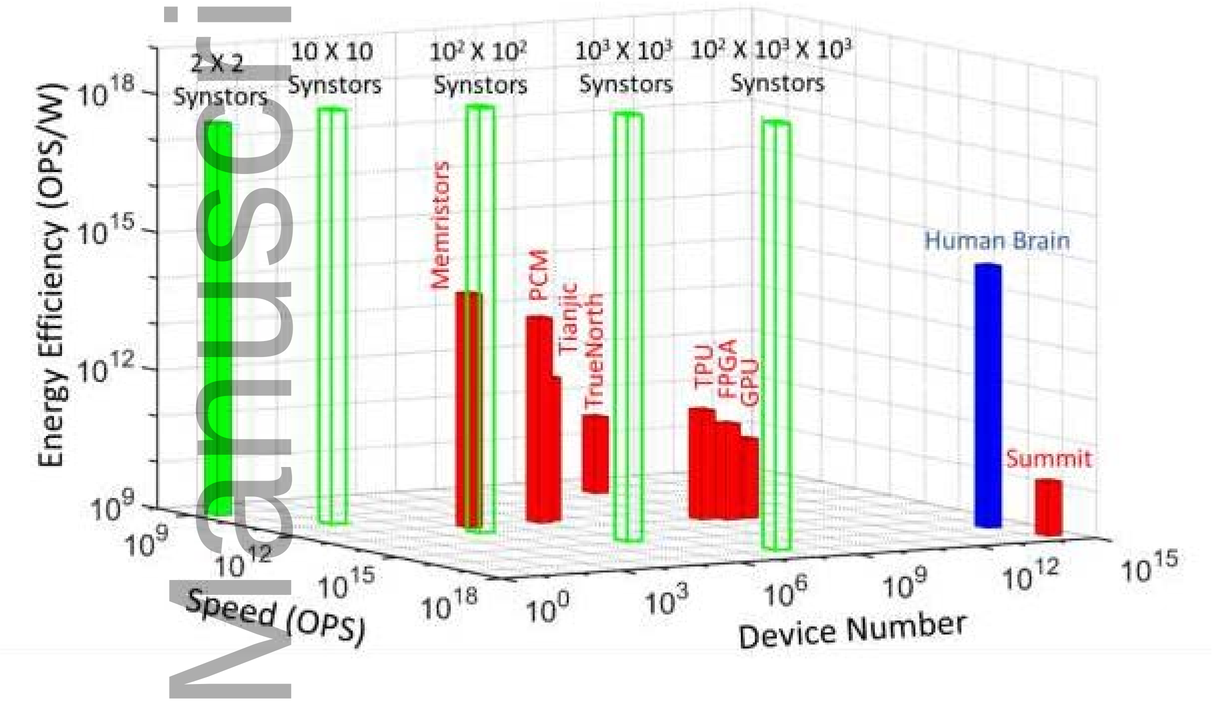

Figure 5. A 3D plot displays the computing energy efficiencies, speeds, and device numbers in a 2 × 2 synstor circuit in this work (green), projected 10×10, $10^2 \times 10^2$, $10^3 \times 10^3$, and $10^2 \times 10^3 \times 10^3$ synstor circuits (green), the human brain (blue), Summit supercomputer, Volta V100 graphics processing units (GPUs) from Nvidia, Stratrix 10 field-programmable gate array (FPGA) from Intel, tensor processing units (TPUs) from Google, TrueNorth neuromorphic circuit from IBM, Tianjic neuromorphic circuits from Tsinghua University, phase change memory circuit from IBM (signal processing only, learning excluded), and memristor circuits from UMass/HP (signal processing only, learning excluded).

Experimental Section

Learning algorithm in a synstor circuit In the self-programming process of a synstor, the feedback pulses, $\boldsymbol{z}$, follow $\boldsymbol{z} = \boldsymbol{y} * \tilde{\theta}$ (Supporting Information, Equation S1), where $\tilde{\theta}(t) = \begin{cases} \theta(t) & when\ -\tau_- < t < 0 \\ -\theta(t) & when\ \tau_+ > t > 0 \\ 0 & when\ t = 0\ or\ t \geq \tau_+\ or\ t \leq -\tau_- \end{cases}$, the time constants $\tau_+ > 0$ and $\tau_- > 0$, the function $\theta(t) > 0$. The average $\tilde{\theta}$ over learning period T, $\langle \tilde{\theta} \rangle = 0$, and the average $\boldsymbol{z}$ over learning period T, $\langle \boldsymbol{z} \rangle = 0$, and $\tilde{\boldsymbol{z}} = \boldsymbol{z} - \bar{\boldsymbol{z}} = \boldsymbol{z}$. To generate feedback pulses with $z_n = y_n * \tilde{\theta}$, a train of positive (negative) feedback pulses with a pulse firing rate proportional to $\theta(t - t_n)$ within the time window $t_n - \tau_- < t < t_n$ at the n^th (complimentary) output electrode, and a train of negative (positive) feedback pulses with a pulse firing rate proportional to $\theta(t - t_n)$ within the time window $t_n < t < t_n + \tau_+$ are triggered at the n^th output electrode.

Synstor circuit fabrication: The synstor circuit was fabricated by the process reported previously.[28] Si wafers with a 100 nm thick SiO_2 layer were diced into 3 cm x 3 cm square chips. A 10 µm long and 50 nm thick Al reference electrode (Supporting Information, Figure S1a) was deposited by electron beam (e-beam) evaporation (CHA Industries, CHA Mark 40), and patterned by photolithography and wet chemical etching with tetramethylammonium hydroxide (TMAH) based photoresist developer (AZ 300 MIF Developer). A 22 nm thick HfO_2 barrier layer and a 2.5 nm thick TiO_2 charge storage layer (Supporting Information, Figure S1b) were deposited by atomic layer deposition (Cambridge NanoTech, Fiji Thermal and Plasma ALD). The TiO_2 film was patterned (Supporting Information, Figure S1c) by photolithography and CF_4/O_2 (5:1 pressure) reactive ion etching (Technics RIE) to form a 10 µm long pattern aligned to the Al reference electrode. A 6.5 nm thick HfO_2 barrier layer (Supporting Information, Figure S1d) was deposited by ALD, encapsulating the patterned TiO_2 charge storage layer. The chip surface was coated by an adhesion monolayer of poly (L-lysine) (PLL). A randomly oriented network of semiconducting single walled carbon nanotubes (CNTs) was deposited by immersion coating (Supporting Information, Figure S1e) in an aqueous 99.9% pure semiconducting single walled CNT aqueous solution (Nanointegris, IsoNanotubes-S99.9%). Residual surfactant was removed from the surface by immersion in isopropanol (IPA) for 1 hour, rinsing with IPA, and drying by nitrogen blow dry. CNTs were doped to p-type by adsorbing O_2 acceptors from atmosphere. A 50 nm Al film (Supporting Information, Figure S1f) was deposited by e-beam evaporation and patterned by the same process used for the Al reference electrode to form input and output electrodes. The CNTs were capped by a Parylene-C (PLC) polymer passivation layer deposited (Supporting Information, Figure S1g) by thermal evaporation (Specialty Coating Systems, 2010 Parylene Vacuum Deposition System). The CNT network and PLC layer were patterned by photolithography with SU-8 photoresist and O_2 RIE to form a 20 μm long CNT channel (Supporting Information, Figure S1g). The SU-8 is an etch mask for the CNTs and PLC during O_2 RIE and encapsulates the CNTs and PLC prevent ambient doping of CNTs by atmosphere.

SNIC testing: Voltage pulses, $\boldsymbol{x}$ and $\boldsymbol{z}$, were generated by function generators (Agilent 33250A) with voltage amplitudes ranging between $-2\ V$ to $2\ V$, a duration ranging between $10\ ns$ to $5\ ms$, and a frequency ranging between $50\ MHz$ to $100\ Hz$, and were applied to the input and output electrodes of synstor circuits. The $\boldsymbol{x}$ and $\boldsymbol{z}$ voltage pulses were gated by switches (Maxim, MAX383), which were activated by a digital voltage module (National Instruments, 9403E Digital Input/Output). The synchronized input and output pulses from a single generator prevented phase shifts between the pulses. Output voltage pulses, $\boldsymbol{y}$, were also read by the digital voltage module. The input, output, feedback, actuation, and reference voltage signals were measured by an analog module (National Instruments, 9205 Analog Input). To extrapolate the synstor conductance w, input pulses $x = -1.75\ V$ were applied to a synstor, and the output current from the synstor was measured by an operational amplifier (Microchip Technologies, MPC6022).

Morphing wing: The morphing wing is a wing section with a 12-inch chord and a morphing trailing edge, which uses a macrofiber composite (MFC) piezoelectric actuator and a flexure box mechanism to modify the camber of the trailing edge.[30, 32] The actuator has a 3D printed elastomeric honeycomb skin for tailored stiffness, and the piezoelectric mechanism allows for fast response time. The morphing wing has applications in stall recovery during wind gusts, optimizing the lift distribution to increase aerodynamic efficiency, and reducing turbulence. The design is scalable to multiple piezoelectric actuators along the spanwise edge (spanwise morphing trail edge) to achieve continuous wing shape change, but the hysteresis of the piezoelectric actuator increases the difficulty of controlling the wing, which is adapted by the real-time self-programming functionality of the synstor circuit. The output voltage signals from the synstor circuit, $\boldsymbol{y}$, triggered an analog actuation voltage, V_a, from an analog voltage module (National Instruments, NI-9264). V_a was amplified by a high-voltage driver (Avid LLC, AVID-EHV-MFC.B2) to a range of -0.5 to $1.5\ kV$ to control the piezoelectric actuators and modify the wing shape.

Wind tunnel: The morphing wing was tested in a laminar flow, open circuit wind tunnel (Aerolab) with a 24x24 inch test section. A fan in the wind tunnel was driven by a high voltage driver (ABB, ACS550-01-046A-2 AC) to randomly change wind speed, S, in the range of $17.3\ m/s$ and $28.7\ m/s$. S was measured by a pitot tube and air velocity transducer (TSI, 8455). The lift force on the wing, F, was measured using a force-torque multi-axis load cell (JR3, 30E12A-4-I40-EF 40N3.1S) with a measurement range of $\pm 80\ N$ and resolution of $0.01\ N$, attached to a morphing wing mounting shaft. The sensory signals of S and F were read by a voltage I/O device (National Instruments, PCIe 6353 Multifunction I/O Device).

Human controllers: The $F - \hat{F}$ values were dynamically displayed to the participants, who pressed two keys on a keyboard to increase or decrease the actuation voltage, V_a. The change rate of V_a was determined by the keystrokes, $\dot{V}_a = \rho_h(a_{k1} - a_{k2})$, where $a_{k1} = \begin{cases} 1 & when\ key\ 1\ is\ pressed \\ 0 & when\ key\ 1\ is\ not\ pressed \end{cases}$

and $a_{k2} = \begin{cases} 1 & when\ key\ 2\ is\ pressed \\ 0 & when\ key\ 2\ is\ not\ pressed \end{cases}$, and ρ_h was randomly set to $31\ mV/ms$ or $-31\ mV/ms$ before each experiment started. V_a was modified by the humans to minimize the objective function $E = \frac{1}{2}\left(F - \hat{F}\right)^2$ under the randomly changed wind speed S.

PID controller: The lift force error, $e_F = F - \hat{F}$, was sent to the PID controller to induce the actuation voltage V_a following the PID control algorithm, $\dot{V}_a = K_p e_F + K_i \int_0^t e_F(t')\, dt' + K_d \dot{e}_F$, where K_p denotes the proportional gain, K_i denotes the integral gain, and K_d denotes the derivative gain. After the gains of the PID controller were set to various combinations of $K_p = 10^{-4}$, 10^{-3} , or $10^{-2}\ V/N \cdot s$; $K_i = 10^{-3}$, 10^{-2}, or $10^{-1}\ V/N \cdot s^2$; and $K_d = 10^{-2}$, 10^{-1}, or $1\ V/N$, the PID controller modified V_a and the shape of the wing while experiencing wind with static speed $S = 28.7\ m/s$. The average objective function $\langle E \rangle = \frac{1}{2}\langle\left(F - \hat{F}\right)^2\rangle$ during the control processes is shown as a function of K_p, K_i, and K_d in Supporting Information Figure S7, and $\langle E \rangle$ approaches its minimal value under the optimal gains with $K_p = 10^{-5}\ V/N \cdot s$, $K_i = 10^{-4}\ V/N \cdot s^2$, and $K_d = 10^{-3}\ V/N$. After the PID controller was preprogrammed to the optimal gains, the PID controller modified V_a and the shape of the wing experienced the randomly changed wind speeds S, emulating an unpredictable aerodynamic environment beyond the static wind speed.

SNIC computing speed and energy efficiency: In comparison with computers, the equivalent computing operations in an $M \times N$ synstor circuit are approximately equal to $3MN$ to implement the signal processing algorithm ($\boldsymbol{I} = \boldsymbol{w}\,\boldsymbol{x}$ (Equation 1), $2MN$ for multiplications between $\boldsymbol{w}$ and $\boldsymbol{x}$; MN for accumulations), and $3MN$ to implement the learning algorithm ($\dot{\boldsymbol{w}} = \alpha\, \boldsymbol{z} \otimes \boldsymbol{x}$ Equation 2), $2MN$ outer products between α, $\boldsymbol{x}$, and $\boldsymbol{z}$; MN for $\boldsymbol{w}$ modifications. The speed for the synstor circuit to implement $6MN$ equivalent computing operations for parallel signal processing and learning,

$$V_c = 6MNf_c \qquad (4)$$

where f_c denotes the operation frequency of the circuit. When voltage pulses are applied on its input or output electrode of an $M \times N$ synstor circuit connected with N output integrate-and-fire neuron circuits, the average power consumption in an $M \times N$ synstor circuit,

$$P_c \approx MN\langle w\rangle\, V_a^2 D_p + NE_p\langle r_y\rangle \qquad (5)$$

where $\langle w\rangle$ denotes the average conductance of the synstors, V_a denotes the magnitude of pulses, D_p denotes the average duty-cycle of the pulses, E_p denotes the average energy consumption to trigger a pulse from integrate-and-fire neuron circuits, and $\langle r_y\rangle$ denote the average firing rates of pulses from output neuron circuits. The input neurons are part of the circuit of last layer, so their energy consumption is not included in the SNIC energy consumption of the current layer. The computing energy efficiency of a synstor circuit is equal to its computing speed V_c divided by its power consumption P_c,

$$C_E = 6f_c/(\langle w\rangle V_a^2 D_p + E_p\langle r_y\rangle/M) \qquad (6)$$

The computing energy efficiency of SNIC operated with operation frequency $f_c = 100\ MHz$, average synstor conductances $\langle w\rangle = 10\ nS$, $V_a = 1.75\ V$, $D_p = 0.06$, $E_p = 10\ pJ$, $r_{in} = 300\ kHz$, and $\langle r_y\rangle = 160\ Hz$, is approximately equal to $3.3 \times 10^{17}\ OPS/W$.

Supporting Information

Supporting Information is available from the Wiley Online Library or from the author.

Acknowledgements

The authors acknowledge the support of this work by the Air Force Office of Scientific Research (AFOSR) under the programs, "Avian-Inspired Multifunctional Morphing Vehicle (FA9550-16-1-

0087)” and “Brain Inspired Networks for Multifunctional Intelligent Systems in Aerial Vehicles (FA9550-19-0213)’’.

Received: ((will be filled in by the editorial staff))

Revised: ((will be filled in by the editorial staff))

Published online: ((will be filled in by the editorial staff))

References

[1] D. O. Hebb, *The organization of behavior: a neuropsychological theory*, J. Wiley; Chapman & Hall, New York, USA **1949**.

[2] Y. Dan, M.-M. Poo, *Neuron* **2004**, *44*, 23.

[3] Z. Chen, S. Haykin, J. J. Eggermont, S. Becker, *Correlative learning: a basis for brain and adaptive systems*, Vol. 49, John Wiley & Sons, New York, USA **2008**.

[4] T.-J. Huang, *International Journal of Automation and Computing* **2017**, *14*, 520.

[5] A. Turing, *Mind* **1950**, *59*, 433.

[6] J. Schmidhuber, *Neural networks* **2015**, *61*, 85.

[7] D. Silver, A. Huang, C. J. Maddison, A. Guez, L. Sifre, G. Van Den Driessche, J. Schrittwieser, I. Antonoglou, V. Panneershelvam, M. Lanctot, S. Dieleman, D. Grewe, J. Nham, N. Kalchbrenner, I. Sutskever, T. Lillicrap, M. Leach, K. Kavukcuoglu, T. Graepel, D. Hassabis, *Nature* **2016**, *529*, 484.

[8] R. P. Feynman, *Feynman lectures on computation*, CRC Press, Boca Raton, FL, USA **2018**.

[9] R. Bellman, *Science* **1966**, *153*, 34.

[10] D. Silver, T. Hubert, J. Schrittwieser, I. Antonoglou, M. Lai, A. Guez, M. Lanctot, L. Sifre, D. Kumaran, T. Graepel, T. Lillicrap, K. Simonyan, D. Hassabis, *Science* **2018**, *362*, 1140.

[11] D. Amodei, S. Ananthanarayanan, R. Anubhai, J. Bai, E. Battenberg, C. Case, J. Casper, B. Catanzaro, Q. Cheng, G. Chen, J. Chen, J. Chen, Z. Chen, M. Chrzanowski, A. Coates, G. Diamos, K. Ding, N. Du, E. Elsen, J. Engel, W. Fang, L. Fan, C. Fougner, L. Gao, C. Gong, A. Hannun, T. Han, L. Johannes, B. Jiang, C. Ju, B. Jun, P. LeGresley, L. Lin, J. Liu, Y. Liu, W. Li, X. Li, D. Ma, S. Narang, A. Ng, S. Ozair, Y. Peng, R. Prenger, S. Qian, Z. Quan, J. Raiman, V. Rao, S. Satheesh, D. Seetapun, S. Sengupta, K. Srinet, A. Sriram, H. Tang, L. Tang, C. Wang, J. Wang, K. Wang, Y. Wang, Z. Wang, Z. Wang, S. Wu, L. Wei, B. Xiao, W. Xie, Y. Xie, D. Yogatama, B. Yuan, J. Zhan, Z. Zhu, "Deep speech 2: End-to-end speech recognition

in english and mandarin", presented at *International conference on machine learning*, New York, NY, USA, **2016**

[12] Oak Ridge National Laboratory, America's newest and smartest supercomputer, https://www.olcf.ornl.gov/summit/, accessed: May, **2018**.

[13] Nvidia, Nvidia Tesla V100 GPU architecture, http://images.nvidia.com/content/volta-architecture/pdf/volta-architecture-whitepaper.pdf, accessed: August, **2017**.

[14] N. P. Jouppi, C. Young, N. Patil, D. Patterson, G. Agrawal, R. Bajwa, S. Bates, S. Bhatia, N. Boden, A. Borchers, R. Boyle, P.-l. Cantin, C. Chao, C. Clark, J. Coriell, M. Daley, M. Dau, J. Dean, B. Gelb, T. V. Ghaemmaghami, R. Gottipati, W. Gulland, R. Hagmann, C. R. Ho, D. Hogberg, J. Hu, R. Hundt, D. Hurt, J. Ibarz, A. Jaffey, A. Jaworski, A. Kaplan, H. Khaitan, D. Killebrew, A. Koch, N. Kumar, S. Lacy, J. Laudon, J. Law, D. Le, C. Leary, Z. Liu, K. Lucke, A. Lundin, G. MacKean, A. Maggiore, M. Mahony, K. Miller, R. Nagarajan, R. Narayanaswami, R. Ni, K. Nix, T. Norrie, M. Omernick, N. Penukonda, A. Phelps, J. Ross, M. Ross, A. Salek, E. Samadiani, C. Severn, G. Sizikov, M. Snelham, J. Souter, D. Steinberg, A. Swing, M. Tan, G. Thorson, B. Tian, H. Toma, E. Tuttle, V. Vasudevan, R. Walter, W. Wang, E. Wilcox, D. H. Yoon, "In-datacenter performance analysis of a tensor processing unit", presented at *Proceedings of the 44th Annual International Symposium on Computer Architecture*, New York, USA, **2017**

[15] E. Nurvitadhi, G. Venkatesh, J. Sim, D. Marr, R. Huang, J. Ong Gee Hock, Y. T. Liew, K. Srivatsan, D. Moss, S. Subhaschandra, "Can FPGAs beat GPUs in accelerating next-generation deep neural networks?", presented at *Proceedings of the 2017 ACM/SIGDA International Symposium on Field-Programmable Gate Arrays*, **2017**

[16] P. A. Merolla, J. V. Arthur, R. Alvarez-Icaza, A. S. Cassidy, J. Sawada, F. Akopyan, B. L. Jackson, N. Imam, C. Guo, Y. Nakamura, B. Brezzo, I. Vo, S. K. Esser, R. Appuswamy, B. Taba, A. Amir, M. D. Flickner, W. P. Risk, R. Manohar, D. S. Modha, *Science* **2014**, *345*, 668.

[17] J. Pei, L. Deng, S. Song, M. Zhao, Y. Zhang, S. Wu, G. Wang, Z. Zou, Z. Wu, W. He, *Nature* **2019**, *572*, 106.

[18] K. Kim, C.-L. Chen, Q. Truong, A. M. Shen, Y. Chen, *Advanced Materials* **2013**, *25*, 1693.

[19] C. Diorio, P. Hasler, A. Minch, C. A. Mead, *IEEE transactions on Electron Devices* **1996**, *43*, 1972.

[20] C. Li, M. Hu, Y. Li, H. Jiang, N. Ge, E. Montgomery, J. Zhang, W. Song, N. Dávila, C. E. Graves, Z. Li, J. P. Strachan, P. Lin, Z. Wang, M. Barnell, Q. Wu, R. S. Williams, J. J. Yang, Q. Xia, *Nature Electronics* **2018**, *1*, 52.

[21] T. Berzina, A. Smerieri, M. Bernabò, A. Pucci, G. Ruggeri, V. Erokhin, M. P. Fontana, *Journal of Applied Physics* **2009**, *105*, 124515.

[22] S. Ambrogio, P. Narayanan, H. Tsai, R. M. Shelby, I. Boybat, C. Di Nolfo, S. Sidler, M. Giordano, M. Bodini, N. C. P. Farinha, B. Killeen, C. Cheng, Y. Jaoudi, G. W. Burr, *Nature* **2018**, *558*, 60.

[23] Q. Lai, L. Zhang, Z. Li, W. F. Stickle, R. S. Williams, Y. Chen, *Advanced Materials* **2010**, *22*, 2448.

[24] M. Prezioso, F. Merrikh-Bayat, B. D. Hoskins, G. C. Adam, K. K. Likharev, D. B. Strukov, *Nature* **2015**, *521*, 61.

[25] A. Shafiee, A. Nag, N. Muralimanohar, R. Balasubramonian, J. P. Strachan, M. Hu, R. S. Williams, V. Srikumar, *ACM SIGARCH Computer Architecture News* **2016**, *44*, 14.

[26] R. Kurzweil, *The singularity is near: When humans transcend biology*, Penguin, Viking, NY, USA **2005**.

[27] H. Surden, M.-A. Williams, *Cardozo L. Rev.* **2016**, *38*, 121.

[28] C. D. Danesh, C. M. Shaffer, D. Nathan, R. Shenoy, A. Tudor, M. Tadayon, Y. Lin, Y. Chen, *Advanced Materials* **2019**, *31*, 1808032.

[29] S. Barbarino, O. Bilgen, R. M. Ajaj, M. I. Friswell, D. J. Inman, *Journal of Intelligent Material Systems and Structures* **2011**, *22*, 823.

[30] L. L. Gamble, A. M. Pankonien, D. J. Inman, *AIAA Journal* **2017**, 1.

[31] Y. Chen, *Advanced Intelligent Systems* **2020**, 2000219.

[32] A. Pankonien, Inman, Daniel, *Proc. SPIE 8688, Active and Passive Smart Structures and Integrated Systems* **2013**, *868815*.

The table of contents entry

A synaptic resistor (synstor) circuit emulates the real-time self-programming functionality of the human brain by processing signals and self-programing synstor conductance matrix ***w*** concurrently. The synaptic resistor circuit can potentially circumvent the fundamental limitations of computers, leading to a new intelligent platform to spontaneously improve its performance function *F* in unpredictable and arbitrary environments for artificial general intelligence.

Keyword synaptic resistor, neuromorphic circuit, self-programming, artificial general intelligence

Christopher M. Shaffer, Atharva Deo, Andrew Tudor, Rahul Shenoy, Cameron D. Danesh, Dhruva Nathan, Lawren L. Gamble, Daniel J. Inman, and Yong Chen*

Title: Self-programming Synaptic Resistor Circuit for Intelligent Systems

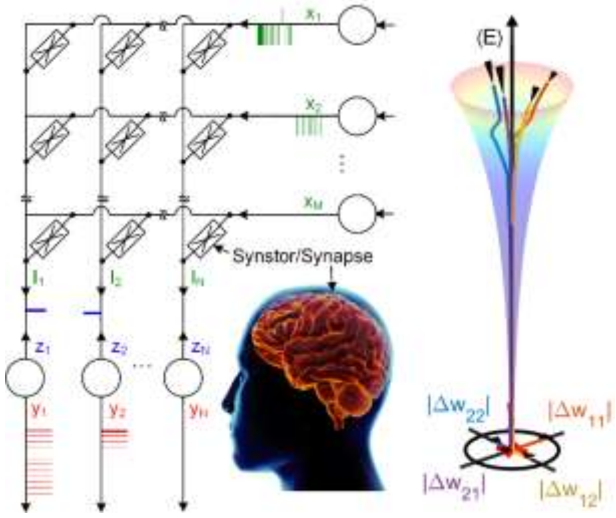

x_1
x_2
x_M
Synstor/Synapse
I_1
I_2
I_N
z_1
z_2
z_N
y_1
y_2
y_N
⟨E⟩
$|\Delta w_{22}|$
$|\Delta w_{11}|$
$|\Delta w_{21}|$
$|\Delta w_{12}|$